Climate Dynamics (2020) 55:277–293
https://doi.org/10.1007/s00382-018-4401-2

Changes in clouds and atmospheric circulation associated with rapid adjustment induced by increased atmospheric CO_2: a multiscale modeling framework study

Kuan-Man Xu[1] · Zhujun Li[2] · Anning Cheng[3] · Yongxiang Hu[1]

Received: 29 December 2017 / Accepted: 12 August 2018 / Published online: 22 August 2018

Abstract
The radiative heating increase due to increased CO_2 concentration is the primary source for the rapid adjustment of atmospheric circulation and clouds. In this study, we investigate the rapid adjustment resulting from an instantaneous doubling of CO_2 and its physical mechanism using a multiscale modeling framework (MMF). The cloud-resolving model component of this MMF includes a sophisticated third-order turbulence closure and the MMF simulates realistic shallow and deep cloud climatology and boundary layer turbulence. Although the simulated cloud adjustment and its mechanism generally agree with earlier studies with conventional global climate models and another MMF with a lower-order turbulence closure, this MMF simulates an increase in the global-mean shortwave and net cloud radiative cooling and a negative cloud radiative effect change due to cloud adjustment. This result is related to the large increase in low-level clouds over the extratropical and subtropical oceans, resulting from reduced cloud-top entrainment implied from strengthened inversion. The downshift of planetary boundary layer and low-level clouds is generally weaker than that simulated by other models, which is due to reduction of shallow cumulus in the ascending and weak subsidence circulation regimes but to increase of stratocumulus in the strongest subsidence regime. Optically thicker stratocumulus compensates for reduced cooling by shallow cumulus. The reduced strength of all oceanic circulation regimes, which may be contributed by weakened energy transport resulting from water vapor and cloud CO_2 masking effects, not only reduces optical depth of convective clouds but also shifts cloud coverage to lands where deep convection is enhanced.

Keywords Rapid adjustment · Low-level clouds · Multiscale modeling framework · Cloud radiative effects · CO_2 forcing

1 Introduction

The climate response to increased CO_2 concentration in the atmosphere consists of direct and indirect effects; the former is the rapid adjustments to increased CO_2 radiative heating while the latter is the slow response to the change of surface air temperature (SAT) caused by increased CO_2 concentration (e.g., Andrews et al. 2010). The slow response is also referred to as the "temperature mediated" change. Rapid adjustments act in a time scale of days and weeks, which is much shorter than that of the slow response (Dong et al. 2009; Cao et al. 2012; Kamae and Watanabe 2013, hereafter, KW13). As long as the CO_2 concentration continues to rise, rapid adjustments will be a crucial contributor to the climate change. It is important to understand rapid adjustments separately from slow response because the changes due to rapid adjustments are often of opposite sign from those of the slow response (e.g., Yang et al. 2003; Andrews et al. 2010; Bony

This paper is a contribution to the special issue on Advances in Convection-Permitting Climate Modeling, consisting of papers that focus on the evaluation, climate change assessment, and feedback processes in kilometer-scale simulations and observations. The special issue is coordinated by Christopher L. Castro, Justin R. Minder, and Andreas F. Prein.

✉ Kuan-Man Xu
Kuan-Man.Xu@nasa.gov

[1] Science Directorate, NASA Langley Research Center, Mail Stop 420, Hampton, VA 23681, USA

[2] NASA Postdoctoral Program, Universities Space Research Association, Hampton, VA, USA

[3] NOAA EMC/NCEP, College Park, MD, USA

et al. 2013; Sherwood et al. 2015). For example, the global-mean precipitation decreases due to abrupt CO_2 increase but it increases over the following years as the global-mean SAT increases in coupled ocean–atmosphere general circulation model (GCM) simulations.

Changes in the atmospheric thermodynamic structure and regional circulation in response to increased CO_2 concentration can cause changes in clouds and the associated changes in the cloud radiative effects (CREs) at the top of the atmosphere (TOA). CREs represent the differences in radiative fluxes between the clear sky and all sky. Zelinka et al. (2013) found that the global-mean CRE change is ~0.5 W m^{-2} from doubling of CO_2 concentration in five atmosphere-only GCM (AGCM) simulations, primarily from shortwave radiation. However, the signs of CRE change vary among GCMs (Gregory and Webb 2008; Webb et al. 2013). The uncertainty in the global-mean CRE change is largely due to that of rapid cloud response, especially the response of low-level clouds (Zelinka et al. 2013). Kamae and Watanabe (2012, hereafter, KW12) and Kamae et al. (2015, hereafter, KWO15) found that the spread of change in the lower-tropospheric specific humidity due to changes in the regional atmospheric circulations can explain most of the spreads in rapid cloud response and the associated CRE change among GCMs. But the governing physical mechanism for this association is not clear (KW12).

A plausible rapid adjustment mechanism that is applicable to the tropical ocean can be described as follows. As the lower-tropospheric temperature over the oceanic regions increases, the lower tropospheric stability (LTS) increases while the surface turbulent heat fluxes decrease. The drying of the lower troposphere (in terms of relative humidity) reduces cloud condensate at the cloud top, while the stabilization of the lower troposphere reduces the cloud top entrainment, resulting in a downward shift of low-level clouds and planetary boundary layer (PBL) height (Wyant et al. 2012, hereafter, WBB12; KWO15). A consequence of this downward shift is a reduction in shortwave (SW) cloud radiative cooling; that is, a positive SW CRE change in the tropical/subtropical subsidence regions where low clouds are abundant. This mechanism, however, does not explicitly consider the contributions from changes in the regional atmospheric circulation and the CO_2 cloud masking effect.

In AGCM simulations of rapid adjustment, the global SAT cannot be held to fixed values although both sea surface temperature (SST) and sea ice concentration are fixed. The smaller heat capacity of the lands allows the SAT to increase more than over the ocean due to the increased downward infrared radiation from the heated troposphere. Such temperature contrasts between the land and oceanic regions alter the regional atmospheric circulation and may shift the cloud coverage from the ocean to lands, which leads to the increase of precipitation over lands (WBB12; KW13; Zelinka et al. 2013; Kamae et al. 2016; Xu et al. 2017). Although the regional circulation response to CO_2 direct radiative forcing is dominated by the CO_2 increase over lands (Shaw and Voigt 2016), the changes in surface sensible heat fluxes due to increased CO_2 concentration can also modulate changes in the regional atmospheric circulation and the hydrological cycle (KWO15; Shaw and Voigt 2016; Xu et al. 2017). Additionally, the plants react to increased CO_2 by closing the stomata and reducing the evapotranspiration of moisture into the atmosphere. Such a response occurs at the same time scale as cloud adjustment. Therefore, it should also impact the adjustment processes (Doutriaux-Boucher et al. 2009; Dong et al. 2009; Andrews et al. 2012).

The direct CO_2 radiative forcing can be weakened by the masking effect of clouds and water vapor in the deep convective regions but enhanced in the drier subtropics (Gregory and Webb 2008; Merlis 2015), where the masking effect is due to cloud (and water vapor) shielding the impact of underlying CO_2 changes. The differential heating resulting from the masking effect reduces energy transport from the convective regions to the subsidence regions or higher latitudes and thus reduces the regional atmospheric circulations. The extent of the weakening of regional atmospheric circulation is related to the dependency of CO_2's radiative forcing on the climatology of cloud and water vapor distributions. Improving the representations of both shallow and deep convective cloud processes is thus important for accurately capturing such masking effects and the associated changes in regional atmospheric circulations, which can lead to a better understanding of physical mechanisms of rapid cloud adjustment. This is due to the fact that traditional GCMs parameterize all cloud physical processes and produce a diversity of low cloud simulations (Soden and Vecchi 2011; Vial et al. 2013) that contribute to the uncertainty of rapid cloud adjustment (Gregory and Webb 2008; Webb et al. 2013; Zelinka et al. 2013) and its physical mechanism (KW12; KWO15).

It has been known for many decades that it is difficult to parameterize the collective effects of convection, clouds, precipitation and radiation in conventional GCMs (Randall et al. 2003). In particular, progress in cloud physical parameterization is slow. Grabowski (2001) and Khairoutdinov and Randall (2001) proposed a multiscale modeling framework (MMF) approach to accelerate the progress. This approach is attractive because each grid column of the global model is embedded with a cloud-system resolving model (CRM). CRM explicitly simulates the cloud scale dynamics. In the past decade, climate change simulations have been performed with MMFs (Wyant et al. 2006; WBB12; Arnold et al. 2014; Bretherton et al. 2014, hereafter, BBS14; Stan and Xu 2014; Xu and Cheng 2016; Xu et al. 2017). The effective climate sensitivity (ECS) is slightly different among the MMFs; 1.5 K (Wyant et al. 2006), 2.1 K (BBS14), and

2.0 K (Xu and Cheng 2016) if a CO_2 doubling forcing of 3.7 W m^{-2} is used (Myhre et al. 1998). ECSs range from 2.1 to 3.0 K for AMIP_4K simulations by conventional GCMs (Ringer et al. 2014), where AMIP_4K stands for Atmospheric Model Intercomparison Project + 4 K SST.

In this study, we adopt the fixed SST approach using an MMF where its CRM component includes a sophisticated third-order turbulence closure as in Cheng and Xu (2011) and Xu and Cheng (2013a, b; hereafter, XC13a, XC13b). This MMF is capable of simulating realistic shallow and deep cloud and water vapor climatology and boundary layer turbulence (XC13a; XC13b; Painemal et al. 2015). We will separately examine the rapid adjustment over the tropical ocean and lands resulting from doubling CO_2 levels except for the precipitation response. Xu et al. (2017) compared the hydrological responses to both CO_2 increase and SST perturbation for two MMFs with or without the higher-order turbulence closure. Similar to conventional GCMs, the land surface temperature in MMF may vary regionally, resulting in differential changes in regional circulation between lands and the ocean. Previous studies noticed less mid-tropospheric subsidence over the tropical lands that may allow more convection and cloud formation in the fixed SST experiments, compared to a fully coupled atmosphere–ocean GCM simulation (Andrews et al. 2012). WBB12 analyzed cloud and circulation response of 2-year-duration MMF simulations to a CO_2 quadrupling. The CRM component of this MMF included a low-order turbulence closure. They identified a shift of cloud coverage and mean large-scale ascent from the tropical ocean to lands, with no effect on global change in cloud cover, and the shoaling of boundary-layer clouds in the subsidence regions (by ~ 80 m), which was also identified in conventional GCMs (KW13).

This study has two objectives: one is to understand rapid adjustments resulting from doubling of CO_2 in the upgraded MMF; and the other is to examine the rapid adjustment mechanisms operating over lands and the ocean as well as different circulation regimes over the tropical ocean. The results from this MMF will be further contrasted to those examined from conventional GCMs and another MMF used in WBB12.

2 Model and experiment design

Both the fixed-SST perturbation and coupled slab-ocean (full ocean) methods have been used in conventional GCMs and MMF to study the response of clouds and atmospheric circulations to CO_2 increase (e.g., Gregory and Webb 2008; Andrews et al. 2012; WBB12; BBS14). However, the former method is more feasible than the latter method for MMF, due to the lengthy spin-up time of an ocean model and computational cost of an MMF relative to that of a conventional GCM (WBB12). Both methods seem to agree on the estimated radiative forcings from the same GCM (Gregory and Webb 2008; Bala et al. 2010; Colman and McAvaney 2011; Andrews et al. 2012) although for the same method the spreads of the cloud radiative forcings are significant among GCMs (KWO15).

The MMF used in this study is SPCAM-IPHOC; superparameterized Community Atmosphere Model (SPCAM) with an intermediately prognostic higher-order turbulence closure (IPHOC) in the embedded CRM (Cheng and Xu 2006, 2011; XC13a). The global model is Community Atmosphere Model (CAM) version 3.5 (Collins et al. 2006). The embedded CRM is the System for Atmospheric Modeling (SAM) (Khairoutdinov and Randall 2003) with IPHOC. The GCM has a horizontal grid spacing of 1.9° × 2.5° and 32 layers in the vertical. Twelve of the 32 layers are located below 700 hPa. These 12 layers are used to resolve the structures of stratocumulus clouds. For comparison, SPCAM only has 6 layers below 700 hPa and its embedded CRM includes a low-order turbulence closure (WBB12; BBS14). The vertical coordinate used in CRMs is identical to that of the host GCM. In the horizontal, there are 32 grid columns with a horizontal grid spacing of 4 km. The CRMs also include cloud microphysics and radiation parameterizations. For interactions between the host GCM and CRMs, tendencies of heat and moisture from the CRM are domain averaged and communicated to the GCM equations. The GCM dynamical core produces the large-scale advective tendencies to drive individual CRMs. The IPHOC package parameterizes sub-CRM-scale variability (Cheng and Xu 2006), as described below.

As in our earlier studies (Cheng and Xu 2011; XC13a), climatological monthly SST and sea ice distributions from Hadley Centre Sea Ice and Sea Surface Temperature dataset (HadISST; Rayner et al. 2003) are specified to the host GCM. There is no interannual variation in SST and sea ice. The integration length of this MMF simulation was 10 years and 3 months, with the last 9 years analyzed. This simulation is referred to as control. For the sensitivity experiment, the CO_2 concentration of the control experiment is instantaneously doubled (Hansen et al. 1984) while the rest of experiment design remain the same as those of the control experiment. The integration length of this experiment was 10 years and 3 months, with the last 9 years analyzed. This simulation is referred to as $2\times CO_2$.

The IPHOC package represents subgrid-scale (SGS) dynamic and thermodynamic variability within a CRM grid box (Cheng and Xu 2006, 2008). A basic assumption is that all SGS variability can be described by a joint double-Gaussian distribution of vertical velocity, liquid–water potential temperature, and total-water mixing ratio. The Gaussian properties of probability density function (PDF) are derived from the first-, second-, and

third-order moments of these three variables. Cloud fraction and grid-mean liquid water mixing ratio are diagnosed from the PDF. The PDF is also used to compute the buoyancy terms and fourth-order terms in the evolution of lower-order moment equations.

Results from the control experiment described above were presented in Cheng and Xu (2013a, b), XC13a, XC13b and Painemal et al. (2015). A major benefit of the IPHOC scheme is that the MMF is capable of simulating the realistic global cloud distributions, including the stratocumulus in the subsidence regions, and the abundance of optically thin clouds. Due to its prediction of three skewness variables, shallow cumulus and its transition to stratocumulus are also well simulated in this MMF. Further, the vertically-integrated water vapor is highly correlated (> 0.98) with observations with a root-mean-square error less than 10% of the global mean (XC13a).

3 Rapid cloud adjustment and changes in the large-scale environment

In this section, we will first discuss the geographic distributions and the global means of selected variables and compare the results with previous SPCAM and conventional GCM studies with similar experimental configurations (Andrews et al. 2012; KW12; WBB12; Zelinka et al. 2013; BBS14; KWO15).

3.1 Changes in surface air temperature (SAT) and cloud

The global mean tropospheric radiative cooling rate is reduced as the CO_2 concentration doubles, especially in the middle troposphere of the tropics (30°S–30°N) between 800 and 500 hPa (Fig. 1b). The global-mean SAT increases by 0.16 K as the land surfaces heat up (Fig. 1a), with the tropical-land SAT increasing by 0.38 K (Table 1). The global-mean SAT increase is about half of the values reported in similar fixed-SST MMF studies with quadrupling CO_2 concentration; 0.30 K in WBB12 for 2-year runs, 0.40 K for years 2–10 and 0.49 K for years 2–30 of long integrations in BBS14. The corresponding tropical-land SAT increases are 0.50 K, 0.77 K and 0.80 K. The weak sensitivity of SAT increase to the integration length after 10 years justifies the use of 10-year integration performed in this study.

The spatial patterns of the land SAT increases are consistent with WBB12, BBS14 and Kamae et al. (2016) for the ensemble mean of 8 conventional GCMs; that is, the SAT increases over most continental areas except for small regions over southern/equatorial Africa, northern South America and western Australia (Fig. 1a). Significant changes in regional circulation are likely responsible for the small SAT changes. It is noted that the warming over the high-latitude lands such as that over the Siberian region is not as strong as in fully coupled GCM simulations with warming in the ocean. The lack of polar amplification is also attributed to the fixed sea ice and SST in the MMF simulations.

A major focus of this study is to understand rapid cloud adjustment. The vertical-horizontal distributions of cloud

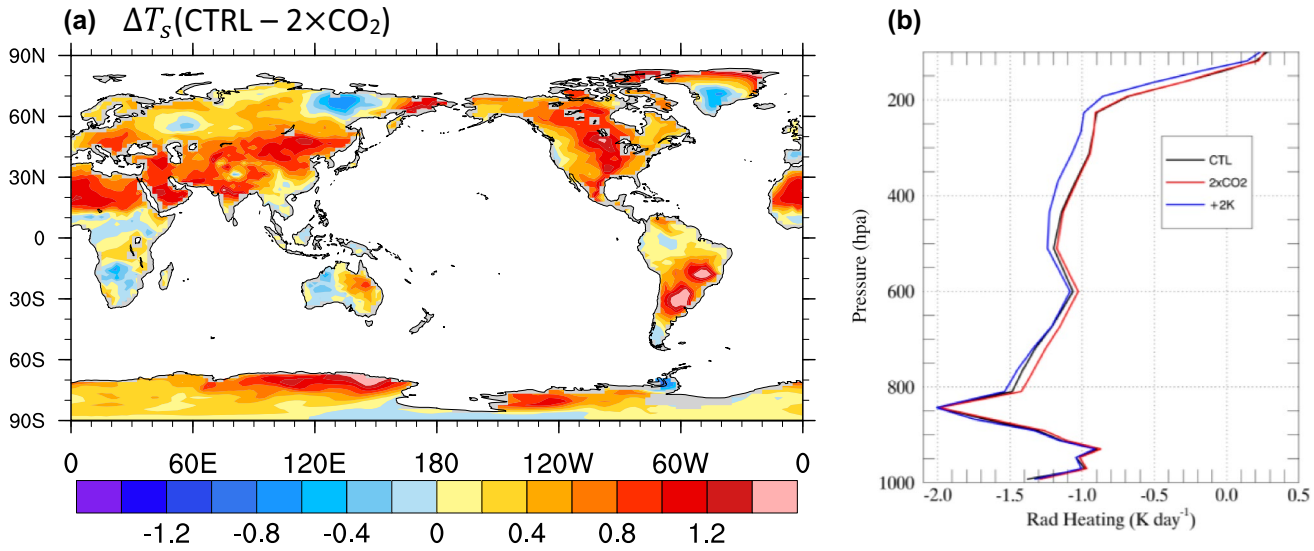

Fig. 1 **a** Annual-averaged surface air temperature change between the $2\times CO_2$ and control experiments. **b** Annual- and tropical-mean profiles of radiative heating rates for the control (CTL; black), $2\times CO_2$ (red) and +2K SST (blue) experiments. The +2K SST experiment is provided for reference although it is discussed in Xu and Cheng (2016) and Xu et al. (2017)

Table 1 The average values over the entire tropics (30°S–30°N), tropical ocean, tropical land, extra-tropics (30°S–60°S, 30°N–60°N) and entire globe for the control experiment as well as the differences between the 2×CO_2 and control experiments

Parameters	Control					2×CO_2—Control					
	Tropics			Extra-tropics	Globe	Tropics			Extra-tropics	Globe	Tropics
	Ocean	Land	Total			Ocean	Land	Total			Total %
T_s (K)	299.2	296.2	298.4	283.8	287.9	0.00	**0.38**	**0.10**	0.16	0.16	0.03
ω_{500} (hPa day^{-1})	−1.76	3.21	−0.46	1.09	0.08	**0.59**	**−2.16**	−0.13	**0.31**	**0.00**	6.0
Low cloud (%)	43.6	20.6	37.5	52.7	45.1	0.0	0.2	0.0	**0.7**	**0.38**	0.1
Middle cloud (%)	8.4	11.8	9.3	24.2	17.2	**−0.2**	**0.4**	−0.1	**−0.4**	**−0.16**	−0.6
High cloud (%)	43.9	25.9	39.1	21.1	29.2	0.7	**1.6**	**1.0**	−0.3	**0.43**	2.4
Total cloud (%)	68.3	40.5	61.0	63.5	61.7	**0.6**	**1.2**	**0.7**	**0.4**	**0.62**	1.2
LWP (g m^{-2})	111.4	70.5	100.7	109.4	98.2	**−2.1**	1.4	**−1.2**	**1.1**	0.13	−1.2
IWP (g m^{-2})	39.2	33.2	37.6	61.4	48.3	−0.3	**2.5**	**0.5**	−0.6	0.11	1.2
Rain (mm day^{-1})	4.02	2.67	3.67	2.4	2.86	**−0.16**	**0.14**	**−0.08**	**−0.1**	**−0.06**	−2.2
LHF (W m^{-2})	150.4	60.6	126.8	61.8	88.5	**−2.3**	0.4	**−1.6**	-0.4	**−0.95**	−1.2
SHF (W m^{-2})	15.6	48.9	24.4	26.7	23.4	**−0.2**	0.3	−0.1	−0.2	−0.11	−0.3
SW CRE (W m^{-2})	−55.8	−40.5	−51.8	−57.7	−50.4	0.3	**−0.9**	0.0	−0.7	−0.39	0.1
LW CRE (W m^{-2})	26.6	20.4	25.0	24.0	22.9	**−0.8**	0.5	**−0.4**	**−0.7**	**−0.47**	−1.8
SW + LW CRE (W m^{-2})	−29.2	−20.1	−26.8	−23.7	−27.5	−0.5	−0.4	−0.4	−1.4	**−0.86**	1.4
SW TOA (W m^{-2})	306.8	282.2	300.4	206.9	240.4	0.3	−0.7	0.0	−0.6	−0.30	0.0
LW TOA (W m^{-2})	259.7	264.6	261.0	229.2	240.3	**−3.9**	**−5.0**	**−4.2**	**−3.0**	**−3.55**	−1.6
TOA LW-SW (W m^{-2})	−47.1	−17.6	−38.6	22.3	−0.1	**−4.2**	**−4.3**	**−4.2**	**−2.4**	**−3.25**	10.9
SW SFC (W m^{-2})	213.9	187.3	207.0	136.5	161.8	0.1	−1.3	−0.2	−0.8	−0.55	−0.1
LW SFC (W m^{-2})	55.9	78.5	61.8	56.6	57.5	**−1.5**	**−2.5**	**−1.7**	**−2.1**	**−1.90**	−2.8
SFC LW-SW (W m^{-2})	−158.0	−108.8	−145.2	−79.9	−104.3	−1.6	−1.2	−1.5	−1.3	**−1.35**	1.0

For ω_{500}, the percentage change is the strength of tropical overturning circulation shown in Table 2. The differences with p value of less than 0.05 from bootstrap tests are in bold

changes between the sensitivity and control experiments will be first examined. Figure 2 shows the low-, middle-, high-level and total cloud amount changes. The low-level clouds are defined as those with tops between the surface and 700 hPa, middle-level clouds with tops between 700 hPa and 400 hPa, and high-level clouds with tops between 400 hPa and the model top. A maximum vertical overlap of cloud fractions between the chosen pressure ranges is used to obtain cloud amount for each CRM grid column. Then, cloud amounts of all CRM columns are horizontally averaged to obtain cloud amount over a GCM grid. The CRM provides cloud fraction at each CRM gridpoint from the double-Gaussian PDF of the IPHOC package.

The global-mean total cloud amount increases by 0.62% (absolute), which is contributed by both low- and high-level clouds (0.38% and 0.43%, respectively). Locally, cloud amount changes from the control to 2×CO_2 experiments exhibit large meridional and zonal variations with values up to 6% (Fig. 2). Most of the global-mean low-level cloud increases are contributed from the extratropical (30°S–60°S and 30°N–60°N) oceans (Fig. 2a; Table 1). Over lands, low-level clouds generally decrease as in conventional GCMs (e.g., Zelinka et al. 2013), such as in America and parts of Europe, which correspond well to the SAT increases, as may be explained by low relative humidity (RH) due to the SAT increase. Low-level cloud amount increases over the rest of land areas where surface temperature experiences small changes (e.g., South Asia, Africa and western Australia). A unique feature of the MMF simulations is the increase of low-level clouds over the subtropics and midlatitudes, in particular, the southeast Pacific and southwest and northeast Atlantic Oceans. These increases compensate for decreases over tropical convective regions and also contribute to the global-mean increase. This feature was not simulated in SPCAM (WBB12; BBS14) and most conventional GCMs (Zelinka et al. 2013).

The global mean middle-level cloud amount decreases by 0.16%, due to the stabilization in the mid-troposphere caused by the CO_2 radiative heating (Fig. 1b). This reduction occurs in both the tropics and higher latitudes and is simulated in all models (e.g., Colman and McAvaney 2011; WBB12; Zelinka et al. 2013), but the magnitude is smaller in this MMF. This is related to the increases in middle-level cloud amount in some regions (Fig. 2b) where there is weak large-scale vertical motion in the control experiment (Fig. 3a) such as Africa (except near the Equator), southern

Table 2 Pressure vertical velocity (ω) and fractional area (σ) at 850 hPa, 700 hPa, 500 hPa and 200 hPa levels for 30°S to 30°N that are obtained for different signs of vertical velocity, upward ($\bar{\omega}^{\uparrow}$, negative) and downward ($\bar{\omega}^{\downarrow}$, positive) of the control experiment

	850 hPa	700 hPa	500 hPa	200 hPa
$\bar{\omega}$	−0.62	−0.65	−0.47	−0.37
$\bar{\omega}^{\downarrow}$	23.43	23.26	22.00	12.41
$\bar{\omega}^{\uparrow}$	−32.00	−33.75	−34.60	−18.35
$I = \bar{\omega}^{\downarrow} - \bar{\omega}^{\uparrow}$	55.43	57.01	56.60	30.76
$\Delta\bar{\omega}^{\downarrow}$	−1.66	−1.73	−1.49	−0.78
$\Delta\bar{\omega}^{\uparrow}$	1.70	1.92	1.92	1.05
$\mathbf{\Delta}I = \Delta\bar{\omega}^{\downarrow} - \Delta\bar{\omega}^{\uparrow}$	−3.36	−3.65	−3.41	−1.83
$\sigma(\omega^{\downarrow})$	0.57	0.58	0.60	0.58
$\sigma(\omega^{\uparrow})$	0.44	0.42	0.40	0.42

*I*represents the strength of tropical overturning circulation. Note that changes between the 2×CO_2 and control experiments ($\Delta\bar{\omega}^{\uparrow}$and $\Delta\bar{\omega}^{\downarrow}$) are calculated over the same areas with upward and downward velocity of the control experiment. The monthly composite (averaged over the same month from years 2–10) data are used to eliminate the changes due to interannual fluctuations. Unit for pressure vertical velocity is hPa day^{-1}

Asia and southern Australia. The magnitudes of subsidence are reduced over the same regions in the 2×CO_2 experiment (Fig. 3c–e), resulting in the increase of both low- and middle-level clouds (Fig. 2a, b). This leads to an increase in albedo. The increase of cloudiness reduces the CO_2 heating in the lower troposphere and thus leads to the small SAT increases over parts of these regions (Fig. 1a) although changes in regional circulation mentioned earlier (Fig. 4) also play an important role in shifting cloud coverage from the ocean to lands.

The largest increases of high-level cloud amount are concentrated over the latitudinal bands over the edges of the tropics as the amount largely decreases over the mid-latitude oceans. This meridional variation signal is more pronounced than that of the zonal variation. The latter is associated with the cloud increases over the land regions such as Africa, southern Asia, Australia and equatorial South America (Fig. 2c), which are well correlated with the increases in upward vertical motion (Fig. 3b, c). The zonal and meridional variations can be explained by circulation (arrows in Fig. 4) and stability changes (colors in Fig. 4) resulting from the CO_2 and water vapor masking effects. These effects weaken the strengths of the Hadley and zonally asymmetric Walker circulations (Merlis 2015). The energy transport from tropical convective regions to higher latitudes, for example, by the mean circulation from the decreased meridional gradient of moist static energy (Fig. 4), is reduced as the middle troposphere over the edges of the subtropics becomes warmer from the CO_2 radiative heating so that the upper troposphere is destabilized (colors in Fig. 4). However, the transport from lands to the adjacent oceans likely increases as the land SAT increases (Figs. 1a, 4), which may impact low-level clouds.

3.2 Changes in cloud radiative effects

Before discussing the CRE changes due to cloud adjustment, the effective radiative forcing (ERF) is examined, which is defined as the sum of net TOA downward SW and longwave (LW) radiative flux changes without any change in global-mean SAT under the conditions of doubled CO_2 (Hansen et al. 2005). In this study, the ERF represents the sum of direct CO_2 forcing and cloud adjustment and is primarily due to reduction of outgoing LW radiative flux (Table 1). The ERF is 3.25 W m^{-2} (TOA SW minus LW) for SPCAM-IPHOC, 3.48 W m^{-2} for SPCAM (BBS14) and 3.77±0.45 W m^{-2} for 13 CMIP5 (Phase 5 of Coupled Model Intercomparison Project) models (KW12), respectively. Therefore, the ERFs of both SPCAM and SPCAM-IPHOC lie at the low end of the range of CMIP5 models although they differ by 0.23 W m^{-2}. As shown in Table 1, the changes in LW CRE are negative for SPCAM-IPHOC (−0.47 W m^{-2}), SPCAM (−0.88 W m^{-2}) and CMIP5 models (−0.76±0.11 W m^{-2}). But the change in SW CRE for SPCAM-IPHOC has an opposite sign (−0.39 W m^{-2} vs. 0.32 W m^{-2} for SPCAM and 0.62±0.24 W m^{-2} for CMIP5 models). This result is related to the large low-cloud increases over the extratropical and subtropical oceans (Fig. 2a), resulting in strong radiative cooling (Fig. 5b). Consequently, the net CRE change for SPCAM-IPHOC (−0.86 W m^{-2}) is more negative, compared to SPCAM (−0.56 W m^{-2}) and CMIP5 models (−0.15±0.26 W m^{-2}) (KWO15). A majority of CMIP5 and earlier-generation models simulated positive SW CRE changes, which were consistent with low-cloud decreases (Gregory and Webb 2008; KW12).

The global-mean CRE changes contain both cloud adjustment and instantaneous cloud masking effects. Utilizing an estimate of cloud masking effects from a conventional GCM (−0.56 W m^{-2}; Andrews et al. 2012), cloud adjustment for SPCAM-IPHOC is −0.30 W m^{-2}, compared to 0.0 W m^{-2} for SPCAM and 0.5 W m^{-2} for conventional GCMs (Zelinka et al. 2013). Because cloud distributions are different among the models, estimates of cloud adjustment with an identical amount of cloud masking effect may be problematic. Nevertheless, the difference in estimated cloud adjustment between the two MMFs can largely explain the difference in ERF (0.23 W m^{-2}).

The magnitudes of local changes in SW CRE can be as large as 10 W m^{-2} while those of LW CRE can be as large as 5 W m^{-2}. The local changes in net CRE are similar to those of SW CRE except for smaller magnitudes (Fig. 5). The net CRE changes are positive (warming) over South and North Americas, and parts of Europe due to decreases of total cloud amount (Fig. 2d), especially those of low-level

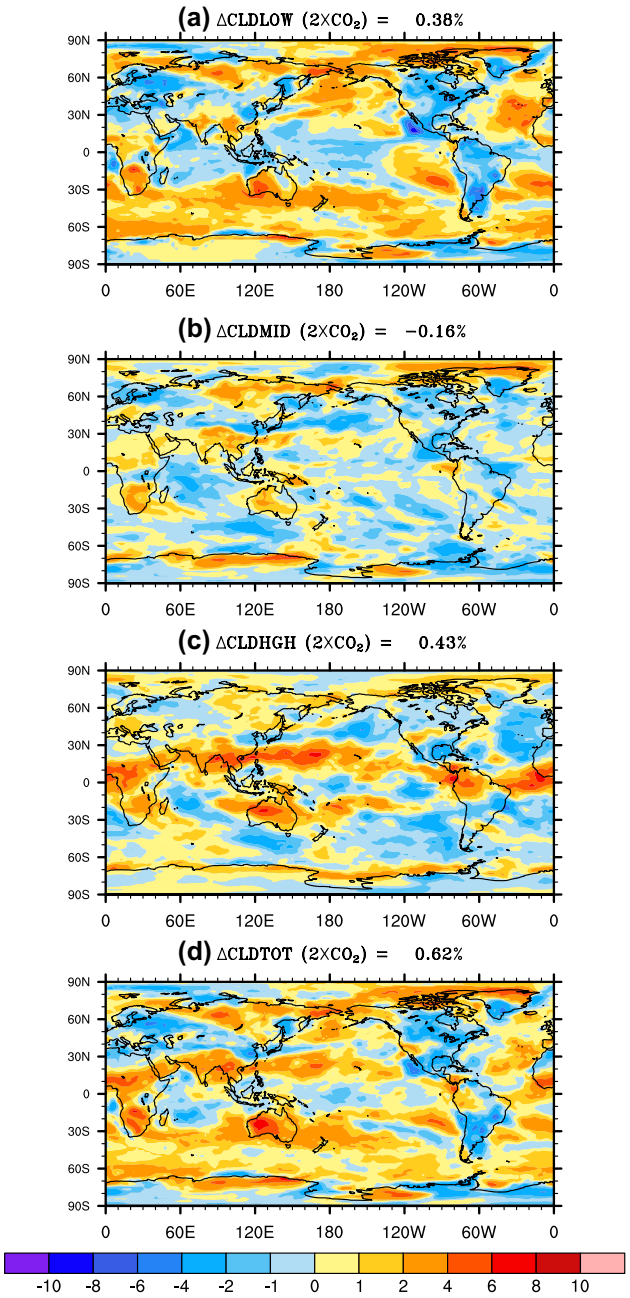

Fig. 2 Global distribution of annual-mean **a** low-, **b** middle-, **c** high-level, and **d** total cloud amount changes between the $2\times CO_2$ and control experiments

cloud amount (Fig. 2a). This is also the case for tropical convective regions, where the large-scale ascent is weakened (Fig. 3) and clouds at all levels decrease (Fig. 2). On the other hand, the net CRE changes are negative (cooling) in parts of the subtropical and mid- and high-latitude oceans due to increases in low-level cloud amount. Overall, the net CRE changes are more pronounced over lands than over the ocean due to changes in regional circulation and the associated shift of clouds from the ocean to lands (WBB12; Shaw and Voigt 2016). This is still true for cloud adjustment even after the net CRE increases are subtracted by 1–2 W m^{-2} (Fig. 5c) due to strong CO_2 cloud and water vapor masking effects over tropical convective regions (Andrews et al. 2012).

3.3 Changes in the thermodynamic and dynamic environments

The rapid adjustment mechanism discussed in the introduction is characterized by (1) stabilization of the lower troposphere, (2) downward shift of the marine boundary layer, (3) reduction in surface turbulent heat fluxes, and (4) reduction in SW cloud radiative cooling (Colman and McAvaney 2011; Andrews et al. 2012; KW12; KW13; WBB12; KWO15). An important element of this mechanism is the decrease in the boundary-layer height and cloud top entrainment due to strengthened PBL inversion (WBB12). Unlike SPCAM and conventional GCMs, increases in net cloud radiative cooling are simulated in three major low-cloud regions: the southeast subtropical Pacific, the southeast Atlantic regions, and the midlatitude storm track regions (Fig. 5c), which is related to increases in low-level cloud amount, as opposed to decreases in low-level cloud amount as simulated by conventional GCMs (Gregory and Webb 2008; Colman and McAvaney 2011; KW12; Zelinka et al. 2013) except for one of the two GCMs in Watanabe et al. (2012). How do the remaining elements contribute to the increases in both low-level clouds and net cloud radiative cooling? To answer this question, we examine a few environmental variables, with an emphasis on the changes in three regions; i.e., the tropical and subtropical oceanic subsidence regions (Fig. 3a), the tropical convective regions and the tropical lands. The changes in these variables are the primary interest although the climatology of selected variables from the control experiment is also shown in Figs. 3, 6, 7 and 8.

The PBL height is obtained from GCM grid-scale variables using the bulk Richardson number (Holtslag and Boville 1993). Change in the PBL height is affected by changes in both the stability and surface virtual heat flux. Over the tropical and subtropical oceanic subsidence regions, there are small decreases (and no increases anywhere) in the PBL height, typically less than 40 m (Fig. 6b). The shoaling of marine boundary layer is thus consistent with previous studies (WBB12; KW13), but the largest decreases in the PBL height occur near the edges of the subtropics (30°S or 30°N). The decrease averaged over 30°S–30°N is ~20 m, compared to 80 m reported in WBB12 for quadrupling CO_2. Note that 80 m was an average over a ten percentile of the high LTS range.

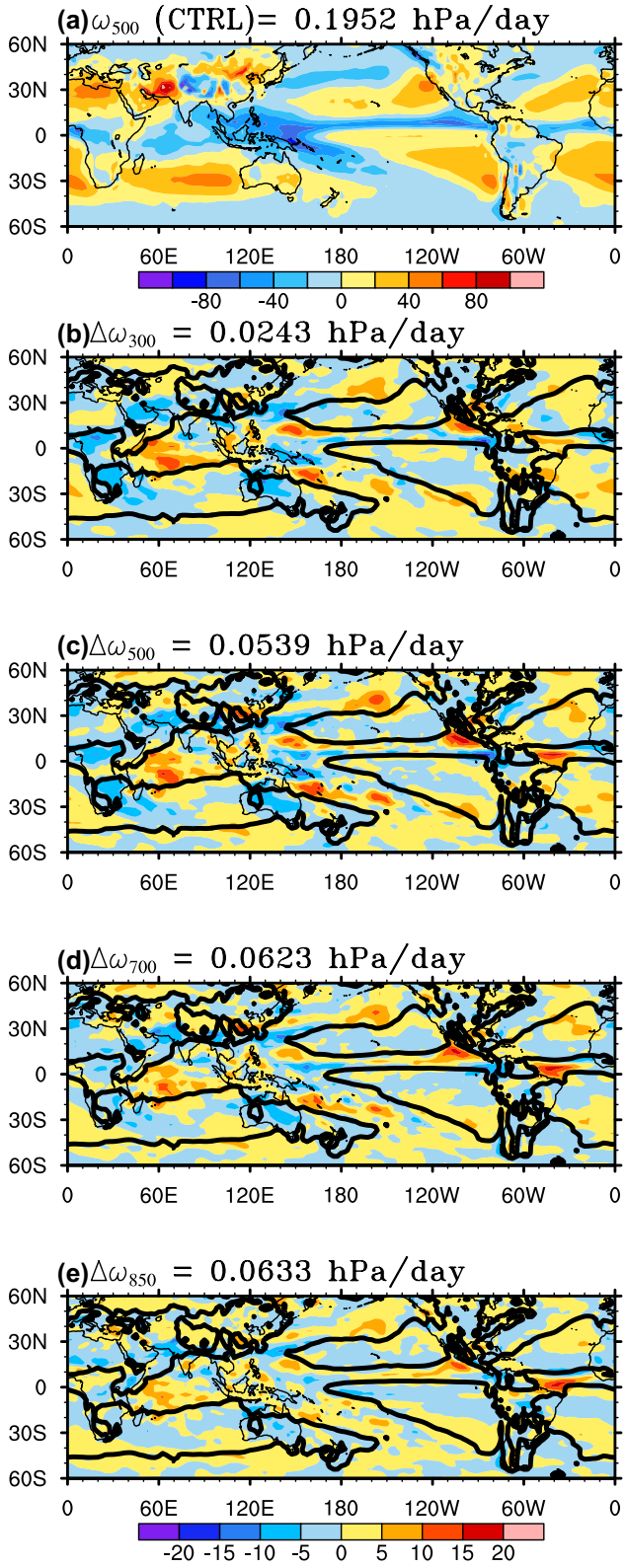

Fig. 3 **a** Distribution of annual-mean pressure vertical velocity at 500 hPa (ω_{500}) for the control experiment, and annual-mean changes in **b** ω_{300}, **c** ω_{500}, **d** ω_{700}, and **e** ω_{850} between the 2×CO_2 and control experiments for 60°S–60°N. The thick black contour in **b**–**e** corresponds to $\omega_{500}=0$

The changes in boundary-layer inversion strength are indicated by those of LTS and estimated inversion strength (EIS). LTS is defined as the deviation of potential temperature at 700 hPa from the surface (Klein and Hartmann 1993) while EIS is similar to LTS except for considering the dependency of moist lapse rate on temperature and providing a more accurate estimate of inversion strength (Woods and Bretherton 2006). Differing from conventional GCMs and SPCAM, the small PBL height decreases are accompanied by increased low-level cloud amount (Fig. 2a), strengthened PBL inversion (Fig. 6d, e) and enhanced LH flux (Fig. 8d). Note that the latter two are shifted westwards and polarward of the strongest subsidence regions (Fig. 3a). Thus, there is a balance between increased entrainment due to turbulent mixing from increased latent heat (LH) flux and decreased entrainment due to (implied from) strengthened PBL inversion. This result can be explained by the higher vertical resolution used in this MMF that reduces artificial entrainment associated with a coarser resolution and limits the jump of cloud top to a smaller height interval (Cheng et al. 2010). The sharper inversion can lead to simulation of more stratocumulus (but with slightly lower tops) with higher liquid water content rather than more cumulus clouds over these regions.

Changes in the large-scale subsidence ($\Delta\omega$) can impact the LTS and RH through the subsidence warming (Fig. 3b–d). In general, changes in ω (at 850 hPa, 700 hPa and 500 hPa) are more variable than those of the LTS. Subsidence in the strong subsidence regions (Fig. 3a), i.e., the southeast subtropical Pacific and Atlantic regions, strengthens/weakened slightly in the 2×CO_2 experiment but the areas with strengthened subsidence shift westwards and polarward from the strong subsidence regions where the LTS increases (Fig. 6d). The RH decreases over these regions and the edges of the subtropics (Fig. 7c, d), which is directly related to the CO_2 radiative heating as the cloud masking effects are weak there. KW12 related the intermodel (conventional GCM) differences in the SW CRE change due to rapid cloud adjustment to those in RH of the subsidence regions. However, the RH decreases of 1–5% do not reduce low-level cloud amounts in these regions, due perhaps to a better simulation of SGS turbulence and cloud processes within the embedded CRMs than with parameterizations in conventional GCMs, which rely on RH to parameterize cloud amount. The RH decreases are also consistent with increased surface LH fluxes (Fig. 8d). This relation may be primarily due to the buoyancy-driven mixing of dry free tropospheric air over a shallower boundary layer that is balanced by increased turbulent mixing from increased LH. This results in a well-mixed boundary layer with lower humidity.

Over most of the tropical lands where surface sensible heat (SH) fluxes increase (Fig. 8b) and the SAT increases (Fig. 1a), the PBL heights increase, up to 100 m (Fig. 6b).

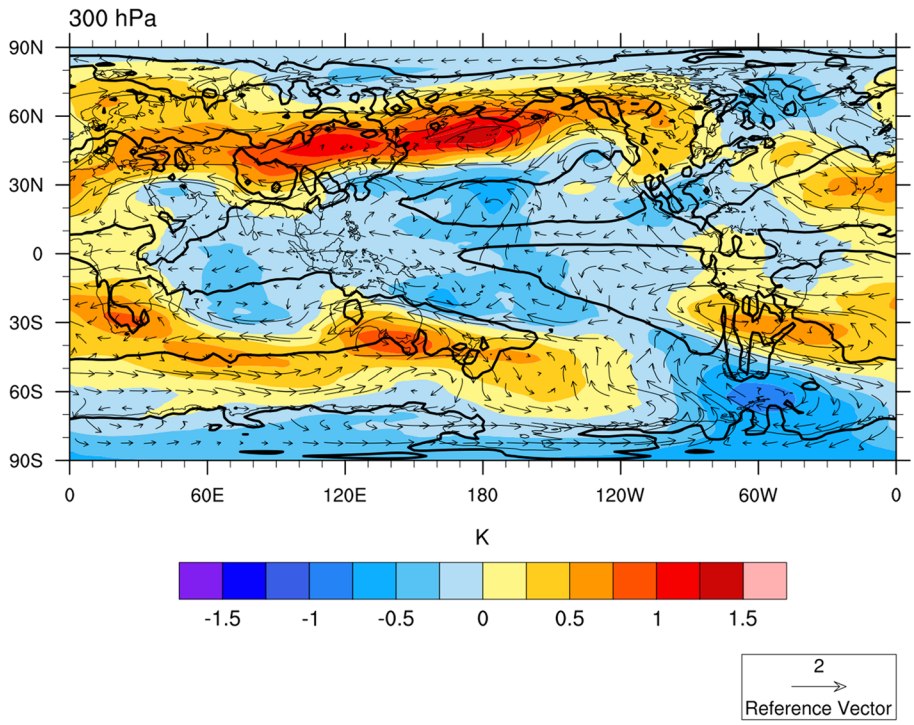

Fig. 4 Global distribution of annual-mean moist static energy (color) and wind (arrow) changes at 300 hPa between the $2\times CO_2$ and control experiments. The thick black contour corresponds to $\omega_{500}=0$. Moist static energy change divided by specific heat capacity (c_p) is shown in color, with unit of K

The exceptions are the South and Central Africa, Australia and part of northwest South America where the small SAT changes reduce the SH fluxes but the LH fluxes increase (Fig. 8d). The LTS decreases over most of the tropical lands (Fig. 6d) are related to the strong increases in the SAT discussed earlier (Fig. 1a). Large-scale ascent is enhanced over most of the tropical lands. Changes in regional atmospheric circulation (Fig. 4) are, thus, an important component of rapid adjustment, as in previous studies (e.g., WBB12; Shaw and Voigt 2016). The RH increases, except for below 700 hPa over North America and parts of South America, are associated with increased deep convection and enhanced large-scale ascent (Fig. 3).

Over tropical deep convective regions (Fig. 3a), neither the LTS (Fig. 6b) nor the PBL height (Fig. 6d) changes much as both are more relevant measures of variability for boundary-layer clouds than deep convection. Large-scale ascent is more likely reduced than enhanced, in particular, the Indian Ocean and northwestern Pacific and western Atlantic (Fig. 3b–e). Since RH changes are closely connected to $\Delta\omega$, there are more areas with decreases than increases in RH because of decreased large-scale ascent strength (to be discussed shortly) and the absolute magnitudes of RH changes increase as the height increases (Fig. 7b–d), as in those of $\Delta\omega$. Additionally, the LH fluxes are reduced in the tropical convective regions (Fig. 8c).

3.4 Changes in circulation strength

As discussed above, regional circulation changes are a driver for cloud changes. A statistical description of the circulation changes can be helpful. The ω_{500} frequencies for both control and $2\times CO_2$ experiments show similar skewed distributions with peaks at 20 hPa day^{-1} (Fig. 9a). Convective regimes correspond to $\omega_{500}< 0$ whereas subsidence regimes correspond to $\omega_{500}\geq 0$. The differences in ω_{500} frequencies between the two experiments confirm the weakening of circulations discussed earlier. This is evidenced by increases in frequency for ω_{500}between -60 hPa day^{-1} (weak-to-moderate ascent) and 20 hPa day^{-1} (weak subsidence) but decreases in frequency for the stronger subsidence regimes ($\omega_{500}>$ 20 hPa day^{-1}) and smaller decreases for the strongly convective regimes (Fig. 9b). Over the tropical lands, there is a clear shift in frequency from the subsidence to convective regimes, which agrees with WBB12. Over the tropical ocean, the weakening of circulation is indicated by increases in frequency for ω_{500}between -40 and 25 hPa day^{-1} and by decreases for the moderately-to-strongly convective regimes ($\omega_{500}<-40$ hPa day^{-1}) and the stronger subsidence regimes ($\omega_{500}>25$ hPa day^{-1}). The decrease for the latter regimes was, however, not simulated by SPCAM (WBB12).

The weakening of circulations can be looked in another way. We compute the average upward ($\bar{\omega}^{\uparrow}$) and downward ($\bar{\omega}^{\downarrow}$) pressure velocities at four selected levels (850, 700, 500 and 200 hPa) for the entire tropics, as well as their difference $I=\bar{\omega}^{\downarrow}-\bar{\omega}^{\uparrow}$, which represents the strength of tropical

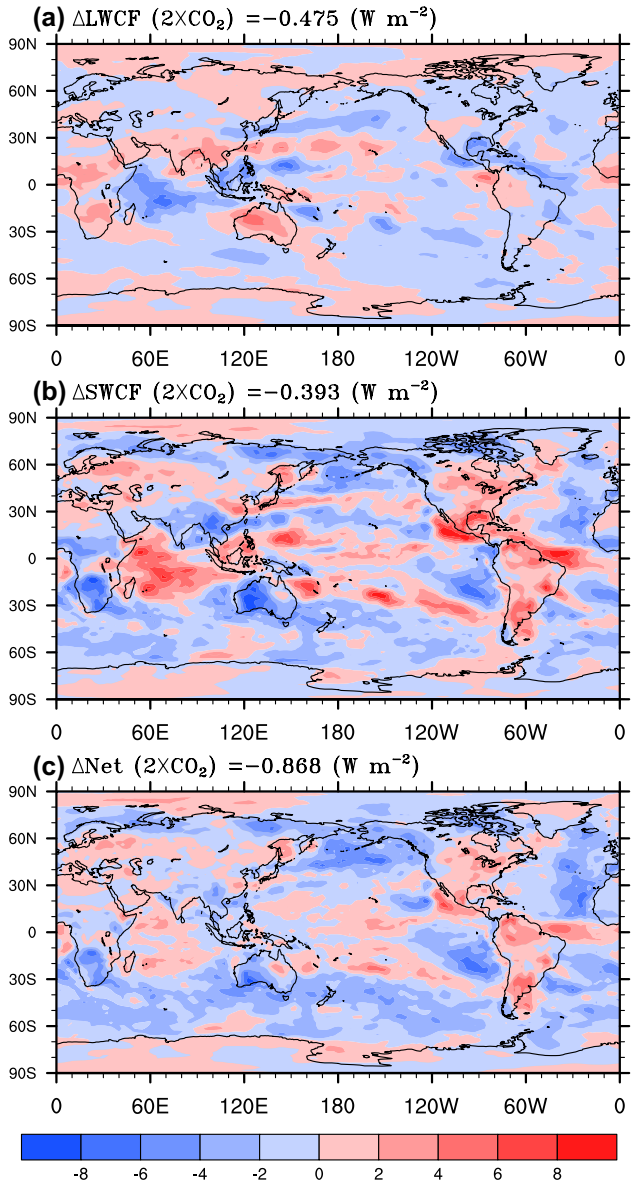

Fig. 5 Global distribution of annual-mean **a** longwave, **b** shortwave and **c** net cloud radiative effect changes between the $2\times CO_2$ and control experiments

overturning circulations (Bony et al. 2013). The average changes in ascending and descending areas of the control experiment ($\mathbf{\Delta}\bar{\omega}^{\uparrow}$ and $\mathbf{\Delta}\bar{\omega}^{\downarrow}$) are also computed (Table 2), using the monthly composite data to exclude the changes due to interannual fluctuations. The largest magnitude in reduced strength of $\bar{\omega}^{\uparrow}$ occurs at 700 and 500 hPa, but that of $\bar{\omega}^{\downarrow}$ occurs at 850 and 700 hPa. The relative weakening, $\Delta I/I$, is similar for all four levels, ranging from 0.059 at 200 hPa to 0.064 at 700 hPa. The weakening of circulation strength is larger over the tropical ocean than over the entire tropics (Bony et al. 2013). This is evident from Fig. 9 for ω_{500}. These results have important implications for understanding the cloud adjustment mechanism.

4 Mechanism of rapid cloud adjustment in the tropics

We will first examine the mean properties over the tropical lands and ocean (Table 1). Statistical significance in the difference between the two experiments is obtained through the bootstrap method. After removing the mean annual cycle of the control experiment, 108 monthly-mean datapoints from either experiment are randomly sampled, with replacement, to create 10,000 subsets from the original datasets. The differences with p value of less than 0.05 are shown in bold in Table 1. The bootstrap test reveals that most mean properties over tropical ocean are different between the two experiments except for low-level cloud amount, TOA SW, surface SW and SW CRE, but over the tropical lands the significant increases of cloud amounts at all levels and cloud ice water path (IWP) significantly increase SW CRE cooling due to the shift of deep convection from the ocean to lands. This shift also makes the oceanic clouds optically thinner due to significant decreases in cloud liquid water path (LWP). The tropical mean results are similar to those of tropical ocean except for SAT, ω_{500}, middle- and high-level cloud amounts, and SH. The lack of significant changes in these five variables except for high-level cloud amount is due to opposite signs in changes between the tropical ocean and lands.

How well do these results compare to those of SPCAM averaged over the same 9-year period (BBS14) after linearly scaling the $4\times CO_2$ changes to $2\times CO_2$ changes? The signs of the changes agree between the two MMFs in ω_{500}, middle-level cloud amount, LWP, IWP, precipitation, TOA and surface SW and LW radiative fluxes, SW and LW CREs and SH for the tropical lands and ocean (Table 3). The disagreement appears in low-level clouds for the tropical lands (+0.2% for SPCAM-IPHOC vs. −0.5% for SPCAM), high and total cloud amounts over the tropical ocean (+0.6 to 0.7% for SPCAM-IPHOC vs. −0.4% for SPCAM). This disagreement does not alter the signs of CRE and TOA and surface radiative flux changes, due to compensation between increased cloud amount and decreased in-cloud cloud optical depth simulated in SPCAM-IPHOC. Thus, the results from SPCAM-IPHOC support the conceptual diagram of rapid cloud changes in the tropics proposed by WBB12 except for the increase of low clouds over lands and the increases of optically thin, high clouds over the ocean, as well as the stronger convection over lands in terms of surface precipitation (0.14 vs. 0.06 mm day^{-1}).

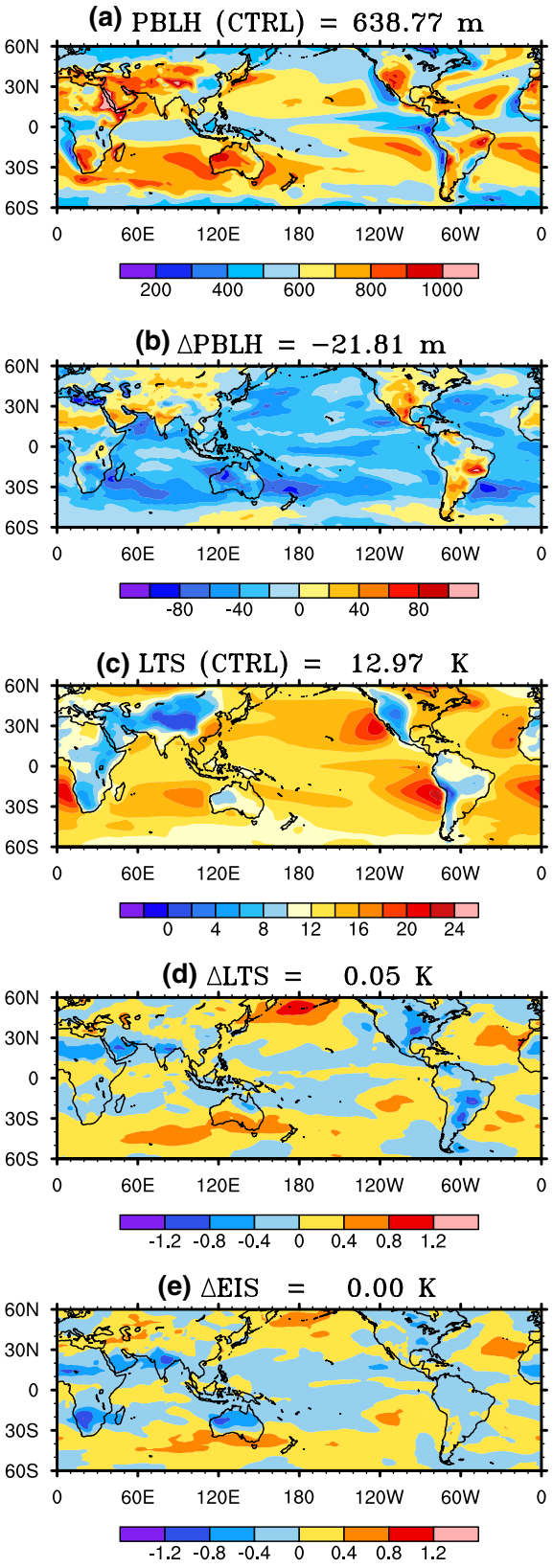

Fig. 6 Distribution of annual-mean **a** PBL height and **c** lower tropospheric stability (LTS) from the control experiment and annual-mean changes in **b** PBL height, **d** LTS, and **e** estimated inversion strength (EIS) between the $2\times CO_2$ and control experiments for 60°S–60°N

4.1 Vertical structure changes over the tropical ocean and lands

Next, vertical profiles of a few variables are obtained for the tropical ocean and lands as in previous studies (WBB12; KW13) to further explain the rapid cloud adjustment mechanism. We also obtain the mean vertical profiles for subregions and circulation regimes. For the tropical lands, the desert region is separated from the rest of tropical lands due to weaker cloud masking effects there. This is chosen as the barren or sparsely vegetated lands (Type 1, Class 16) according to the Moderate Resolution Imaging Spectroradiometer (MODIS) land cover product (MCD12C1), https://lpdata.usgs.gov/dataset_discovery/modis/modis-products-table/mcd12c1.

There are large contrasts in the response to doubling of CO_2 between the tropical ocean and lands and between desert and non-desert regions (Fig. 10). Due to the differences in surface heat capacity, the potential temperature increases ($\Delta\theta$) over lands are 0.1–0.3 K higher than over the ocean while they are ~0.4 K higher over deserts than over non-deserts (Fig. 10b). For the tropical ocean, the negative $\Delta\theta$ in the upper troposphere can be explained by a reduced meridional heat transport (Fig. 4) and less condensational heating resulting from weaker deep convection. The increased stability between the surface and ~800 hPa (Fig. 10b) is accompanied with increased low-level clouds below 850 hPa and significantly reduced condensate amount above 850 hPa (Fig. 10d), reduced $\bar{\omega}^{\downarrow}$ (Fig. 10c), increased humidity within the boundary layer (Fig. 10e), and reduced LH (Table 3). The humidity increase is sufficiently large to compensate for the relative humidity reduction due to warming except near the boundary layer top (Fig. 10f–g). This result is qualitatively consistent with earlier studies (WBB12 and KWO15). Conventional GCMs also show an increase in marine boundary-layer cloud fraction at below ~900 hPa (Zelinka et al. 2013) instead of below 850 hPa in this study. This difference may be related to either stronger downward radiative heating resulted from quadrupling CO_2 or artificially strong entrainment resulted from the coarser resolution in the lower troposphere used in GCMs, or deficiencies in GCM parameterizations.

Over lands, the increased instability corresponds well with enhanced upward motion (up to -2.5 hPa day^{-1}). Over deserts with low heat capacity, $\Delta\omega$ is "bottom heavy," which is related to the large instability increase in the lower troposphere (Fig. 10b). Increased strength of deep convection can be seen from $q_c + q_i$ (condensate mixing ratio) increases over the entire troposphere except for the lower troposphere below 900 hPa (Fig. 10d), which is also accompanied by the large humidity increases (Fig. 10e) that are sufficiently large to compensate for the relative humidity reduction due to warming (Fig. 10f–h). The reduced low-level clouds below

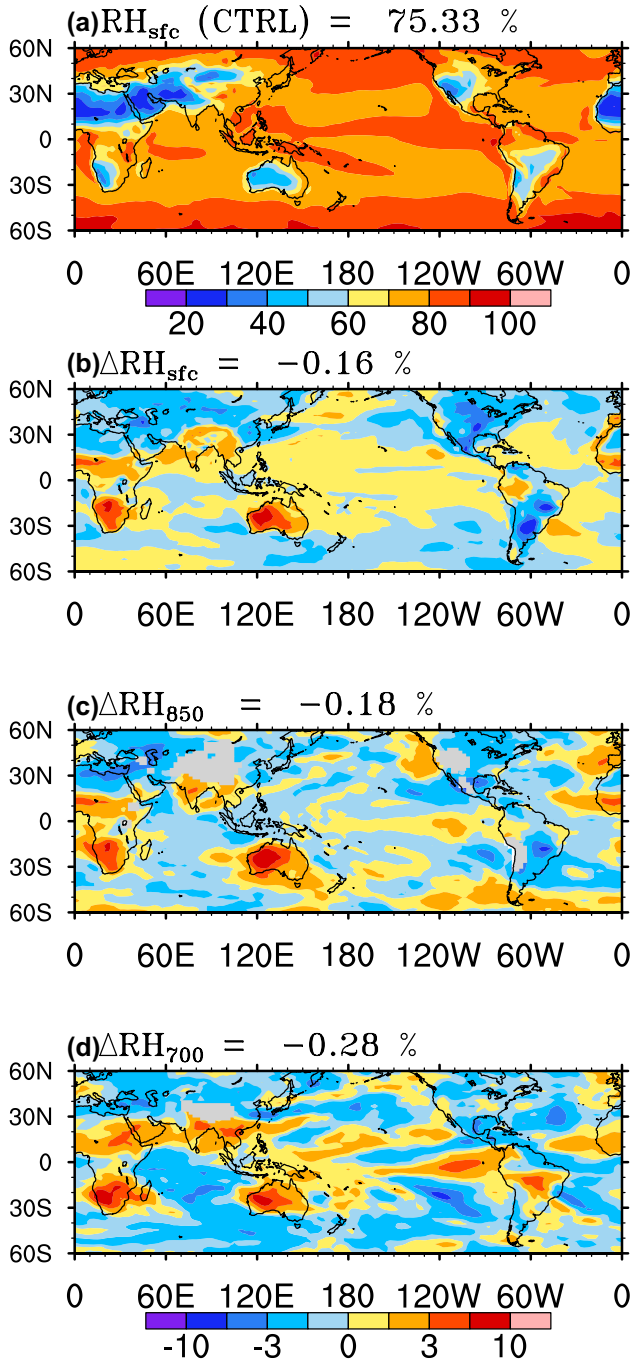

Fig. 7 Distribution of **a** annual-mean relative humidity at first model level from the control experiment and annual-mean changes **b** at first model level, **c** 850 hPa and **d** 700 hPa between the 2×CO_2 and control experiments for 60°S–60°N

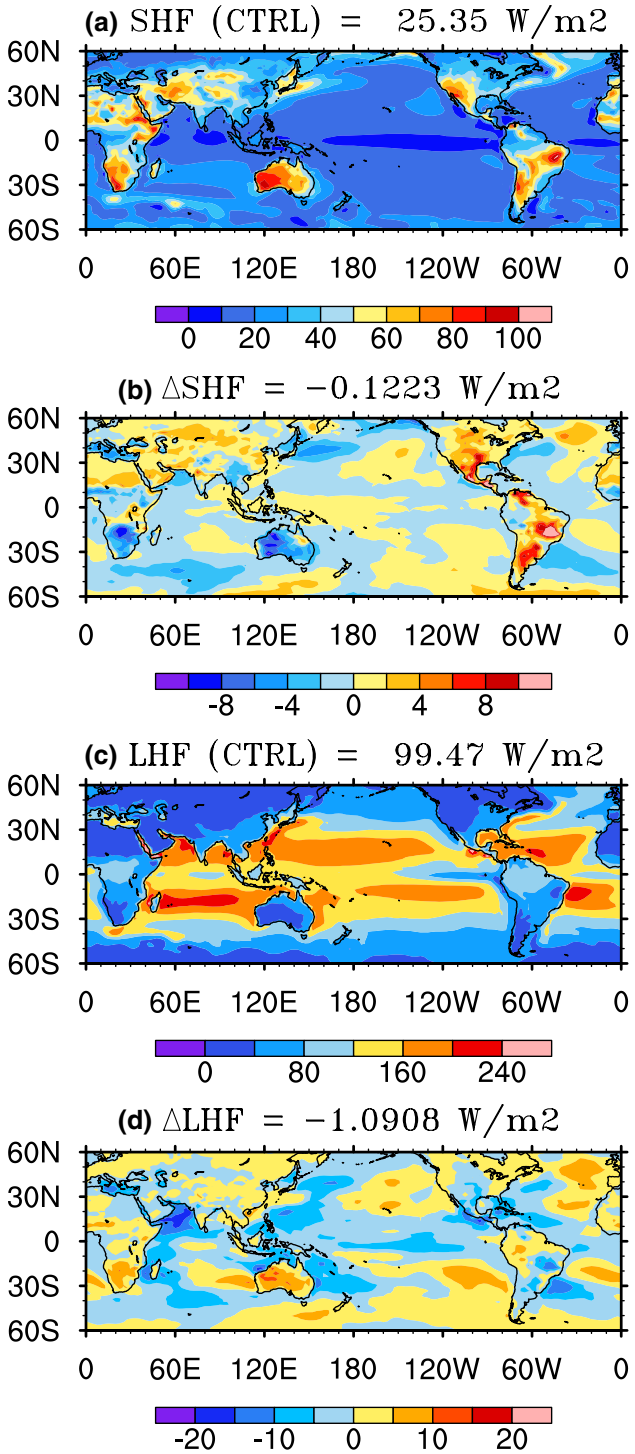

Fig. 8 Distribution of annual-mean **a** sensible heat (SH) and **c** latent heat (LH) fluxes from the control experiment and their annual-mean changes **b, d** between the 2×CO_2 and control experiments for 60°S–60°N

900 hPa are related to the raised PBL height due to stronger turbulent mixing. Despite of this reduction, both condensate mixing ratio and RH between 900 and 775 hPa increase (less so over desert lands). This result is related to the efficient turbulent mixing simulated in this MMF that is supported by the small increases in surface LH and SH fluxes, compared to SPCAM (Table 3) that has a large increase in SH but a large decrease in LH. Thus, SPCAM-IPHOC also simulates enhanced low clouds, except for those below 900 hPa,

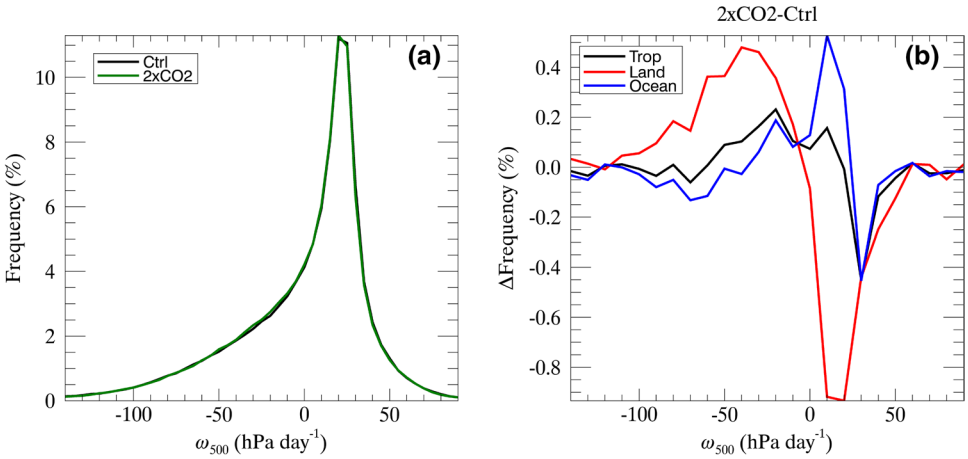

Fig. 9 **a** The frequency (%) of monthly-mean midtropospheric pressure velocity (ω_{500}) over the entire tropics for the control (black) and 2×CO_2 experiments (green) and **b** the difference in frequency between the 2×CO_2 and control experiments for the entire tropics (black), tropical land (red) and tropical ocean (blue). The bin size is 5 hPa day^{-1}

while SPCAM simulates reduced low clouds, as the land surface with more moisture warms up less over non-deserts in SPCAM-IPHOC.

4.2 Vertical structure changes for the tropical oceanic circulation regimes

For the tropical ocean, vertical profiles for five circulation regimes are further examined to further understand the cloud adjustment mechanism. The five circulation regimes with equal size of population (20%), called "quintiles," are obtained, based upon the distribution of annual-mean ω_{500} of the control experiment (Fig. 9a). The ω_{500}ranges of the five quintiles are $\omega_{500} < -21$ hPa day^{-1} (0–20%), $-21 \le \omega_{500} < -4$ hPa day^{-1} (20–40%), $-4 \le \omega_{500} < 10$ hPa day^{-1} (40–60%), $10 \le \omega_{500} < 21$ hPa day^{-1} (60–80%) and $\omega_{500} \ge 21$ hPa day^{-1} (80–100%), respectively. The first two quintiles correspond to strongly and weakly convective regimes while the last three quintiles correspond to weak, moderate and strong subsidence regimes, respectively.

The weakening of regional circulations over the tropical ocean as seen from Fig. 10c is achieved through a large reduction in the ascent strength of convective regimes (up to 2 hPa day^{-1}) and a small reduction in the subsidence strength in the low and middle troposphere of the 1st and 2nd quintiles (up to 1 hPa day^{-1}; Fig. 11c). The ascent strength of the 1st quintile is reduced more greatly in the low and middle troposphere than that of the 2nd quintile, but the reduction in the upper troposphere is similar. The reduction of subsidence strength of the 4th quintile is twice as large as that of the last quintile, which has the strongest subsidence strength.

Although the five circulation regimes have various characteristics in the profiles of thermodynamic/cloud/radiative changes (Fig. 11), the strongest subsidence regime is

Table 3 The average differences over the entire tropics, tropical ocean and tropical lands between the 2×CO_2 and control experiments from the ensemble of CMIP5 models (Kamae and Watanabe 2012), SPCAM (Bretherton et al. 2014) and SPCAM-IPHOC

	CMIP5 Ensemble			SPCAM			SPCAM-IPHOC		
	Ocean	Land	Tropics	Ocean	Land	Tropics	Ocean	Land	Tropics
ω_{500} (hPa day^{-1})	0.43	−0.96	0.08	0.60	−1.98	−0.06	0.59	−2.16	−0.13
Total cloud (%)	−0.4	−0.3	−0.4	−0.4	0.4	−0.2	0.6	1.2	0.7
Low cloud (%)				−0.1	−0.5	−0.2	0.0	0.2	0.0
Middle cloud (%)				−0.3	0.6	−0.1	−0.2	0.4	−0.1
High cloud (%)				−0.4	1.0	−0.1	0.7	1.6	1.0
LWP (g m^{-2})				−2.7	0.9	−1.8	−2.1	1.4	−1.2
IWP (g m^{-2})				−0.7	2.4	0.1	−0.3	2.5	0.5
Rain (mm day^{-1})				−0.16	0.06	−0.10	−0.16	0.14	−0.08
LHF (W m^{-2})				−2.8	−2.7	−2.8	−2.3	0.4	−1.6
SHF (W m^{-2})				−0.2	1.7	0.3	−0.2	0.3	−0.1
SW CRE (W m^{-2})	0.7	0.4	0.6	1.1	−0.8	0.6	0.3	−0.9	0.0
LW CRE (W m^{-2})	−1.1	−0.1	−0.8	−1.5	0.7	−0.9	−0.8	0.5	−0.4
SW TOA (W m^{-2})				1.1	−0.4	0.7	0.3	−0.7	0.0
LW TOA (W m^{-2})				−2.9	−5.0	−3.5	−3.9	−5.0	−4.2
SW SFC (W m^{-2})				1.1	−0.7	0.7	0.1	−1.3	−0.2
LW SFC (W m^{-2})				−1.0	−1.9	−1.2	−1.5	−2.5	−1.7

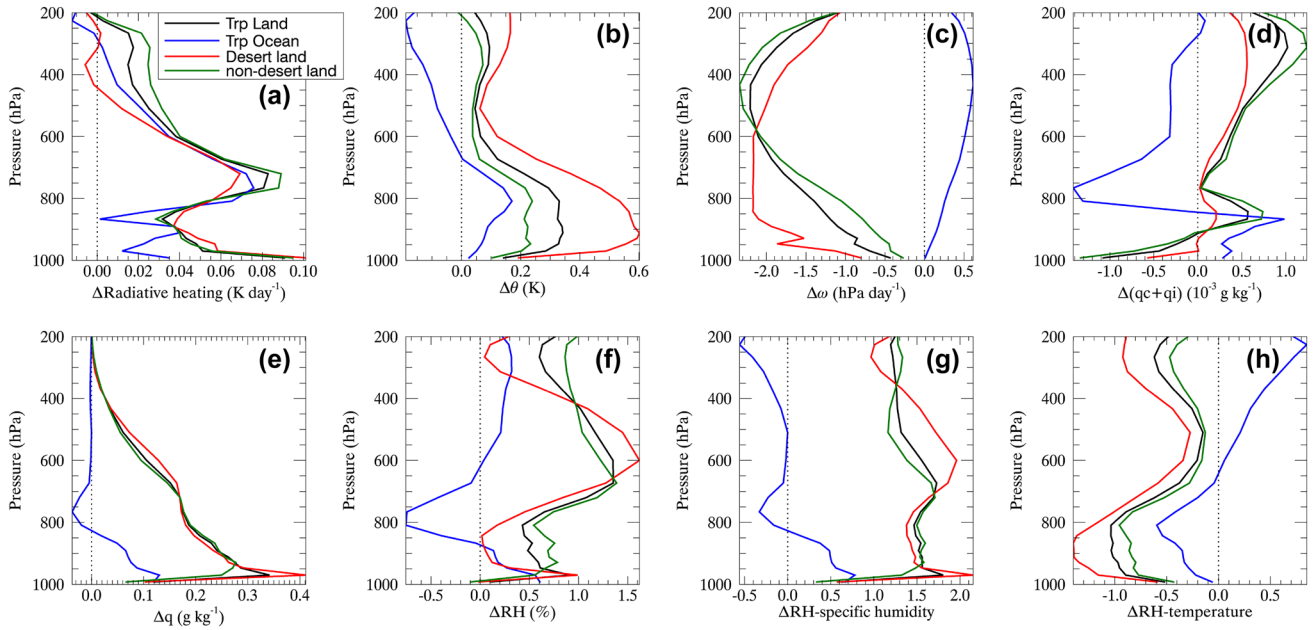

Fig. 10 Vertical profiles of changes in **a** radiative heating rate, **b** potential temperature, **c** pressure vertical velocity, **d** sum of cloud water and cloud ice mixing ratio, **e** specific humidity, **f** relative humidity, **g** relative humidity due to changes in specific humidity and **h** relative humidity due to changes in temperature averaged over the tropical lands, tropical ocean, tropical deserts and tropical non-deserts between the $2\times CO_2$ and control experiments

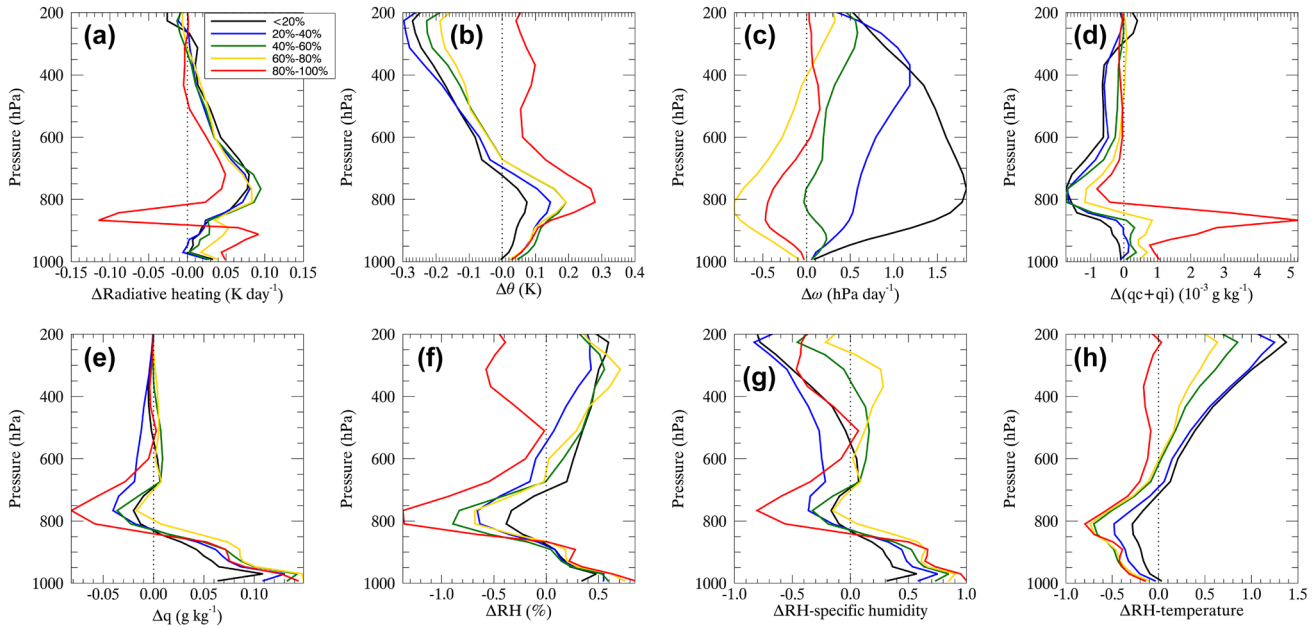

Fig. 11 Same as Fig. 10 except for the tropical ocean profiles sorted by annual-mean ω_{500}, with each color representing the average for 20% of ω_{500} values (or quintile). The 20%, 40%, 60% and 80% thresholds of ω_{500} are roughly -21 hPa day^{-1}, -4 hPa day^{-1}, 10 hPa day^{-1}, and 21 hPa day^{-1}

most distinct and influences the tropical-ocean mean cloud changes between the two experiments discussed earlier (Fig. 10d). This circulation regime has the largest stability increase between the surface and 800 hPa (Fig. 11b), which implies for decreased cloud top entrainment and turbulent mixing in the boundary layer, as also indicated by the cloud top radiative cooling increase (Fig. 11a). Note that the condensate reduction above 800 hPa is minimal for this regime,

compared to the rest of circulation regimes (Fig. 11d). The condensate reduction above 850 hPa in the tropical-ocean mean profile (Fig. 10d) is manifested by a reduction in condensate appearing in the layer above 840 hPa of the other four regimes. The downward shift of low-level clouds seen in the tropical-ocean mean profile is, therefore, associated with all regimes except for the strongest subsidence regime. That is, shallow cumulus clouds within these four regimes are likely reduced, not the stratocumulus clouds in the strongest subsidence regime. If there were no large condensate increase in the strongest subsidence regime, the tropical mean condensate profile would be similar to what other models produced, i.e., much stronger downshift of low-level clouds. Note that the 1st quintile shows the greatest reduction in the vertical extent and amount of condensate (Fig. 11d), which is related to weakened oceanic deep convection.

5 Summary and discussions

In this study, we have investigated the rapid adjustment resulting from doubling of atmospheric CO_2 concentration and its physical mechanism using a multiscale modeling framework (MMF). The CRM component of this MMF includes a sophisticated higher-order turbulence closure. The MMF simulates realistic shallow and deep cloud climatology and boundary-layer turbulence, in comparison with conventional GCMs and SPCAM MMF. This ability is important for simulating rapid adjustment because CO_2—induced cloud and water vapor masking effects, which depend on cloud and water vapor climatology, impact the regional circulations and cloud changes (Merlis 2015).

The simulated cloud adjustment and its mechanism generally agree with earlier studies with conventional GCMs and another MMF in many aspects; for example, the simulated global cloud distributions from this MMF show a decrease in middle-level cloud amount, an increase in high-level cloud amount and a shift of deep convection from the tropical ocean to lands resulting in optically thinner clouds over the ocean and optically thicker clouds over lands, as well as a reduction of circulation strength in response to CO_2 warming. The most significant difference from the earlier studies is that this MMF simulates an increase in the global-mean shortwave and net cloud radiative cooling and a negative net CRE change due to cloud adjustment. This result is related to the large increase in low-level cloud amount occurring over the extratropical and subtropical oceans, resulting from reduced cloud-top entrainment that is implied from strengthened PBL inversion shown in the LTS and EIS spatial distributions.

For cloud adjustment mechanism, the downshift of planetary boundary layer and low clouds simulated in this MMF is generally weaker than that of conventional GCMs and SPCAM MMF. The downshift is due to reduction of shallow cumulus in the ascending and weak subsidence circulation regimes with minimal contribution from stratocumulus in the strongest subsidence regime. The PBL inversion strength of the strongest subsidence regime between the surface and 800 hPa increases the most and thus the entrainment is reduced and clouds are optically thicker. This regime exerts the strongest influence on the tropical-ocean mean cloud changes between the two experiments. Without the contribution from this regime, the tropical mean condensate profile would be similar to what conventional GCMs and SPCAM produced, which is characterized by a much stronger downshift of low-level clouds. The implication of these results is that the embedded CRMs with IPHOC more likely simulate stratocumulus clouds rather than cumulus clouds for the strongest subsidence regime. The high vertical resolution in the lower troposphere used in this MMF also helps to reduce artificial entrainment and minimizes the extent of the PBL shoaling (Cheng et al. 2010; XC13a).

Changes in regional circulation, with strongest reductions in the moderate subsidence and strongly convective regimes, play an important role in influencing oceanic cloud changes and shift of cloud coverage from the ocean to lands. Weaker energy transport resulting from CO_2 cloud and water vapor masking effects in the oceanic regions with strong large-scale ascent reduces the upward motion and convective clouds. Over lands, large-scale upward motion is enhanced throughout the entire troposphere, accompanied by increased moisture related to efficient turbulent mixing. Due to differences in surface heat capacity between desert and non-desert regions, low-level clouds over non-deserts increases rather than decreases over deserts. Deep convection is also enhanced more over non-deserts than over deserts. Large increases of moisture over lands are related to the land–ocean transports that are linked to the different signs of surface SH and LH flux changes (DeAngelis et al. 2016). This MMF simulates small increases in both SH and LH over the tropical lands, compared to large increases in SH but large decreases in LH in SPCAM. The increased moisture over lands increases the low-level clouds and intensity of deep convection and produces more precipitation, compared to SPCAM.

The rapid adjustment mechanism examined in this study may need further investigation because some of the differences from previous studies may be related to nonlinearity in the responses between doubling and quadrupling of CO_2 and to the coarser vertical resolutions used in other studies. However, the MMF results presented in this study will be helpful to further advance our understanding of rapid adjustment simulated in conventional GCMs. The differences between the parameterized and explicitly simulated cloud processes, especially for the strongest subsidence

circulation regime, need to be understood in single-column framework (Randall et al. 1996) and fully ocean–atmosphere coupled models (e.g., Stan and Xu 2014).

Acknowledgements The authors acknowledge the support of NASA Interdisciplinary Study program (Grant No. NNH12ZDA001N-IDS) and NASA Data for Operation and Assessment (Grant No. NNH16ZDA001N-NDOA). We also acknowledge the computational resources from Argonne National Laboratory and the Langley Research Center computation clusters: K-cluster and Icluster. ZL was supported by NASA Postdoctoral Program.

References

Andrews T, Forster PM, Boucher O, Bellouin N, Jones A (2010) Precipitation, radiative forcing and global temperature change. Geophys Res Lett 37:L14701. https://doi.org/10.1029/2010GL043991

Andrews T, Gregory JM, Forster PM, Webb MJ (2012) Cloud adjustment and its role in CO_2 radiative forcing and climate sensitivity: a review. Surv Geophys 33:619–635. https://doi.org/10.1007/s10712-011-9152-0

Arnold NP, Branson M, Burt MA, Abbot DS, Kuang Z, Randall DA, Tziperman E (2014) The effects of explicit atmospheric convection at high CO_2. Proc Natl Acad Sci USA 111:10,943–10,948. https://doi.org/10.1073/pnas.1407175111

Bala G, Calderia K, Nemani R (2010) Fast versus slow response in climate change: implications for the global hydrological cycle. Clim Dyn 35:423–434

Bony S, Bellon G, Klocke D, Sherwood S, Fermepin S, Denvil S (2013) Robust direct effect of carbon dioxide on tropical circulation and regional precipitation. Nat Geosci 6:447–451. https://doi.org/10.1038/NGEO1799

Bretherton CS, Blossey PN, Stan C (2014) Cloud feedbacks on greenhouse warming in the superparameterized climate model SPCCSM4. J Adv Model Earth Syst. https://doi.org/10.1002/2014MS000355

Cao L, Bala G, Caldeira K (2012) Climate response to changes in atmospheric carbon dioxide and solar irradiance on the time scale of days to weeks. Environ Res Lett 7(015):34. https://doi.org/10.1088/1748-9326/7/3/034015

Cheng A, Xu K-M (2006) Simulation of shallow cumuli and their transition to deep convective clouds by cloud-resolving models with different third-order turbulence closures. Q J R Meteor Soc 132:359–382

Cheng A, Xu K-M (2008) Simulation of boundary-layer cumulus and stratocumulus clouds using a cloud-resolving model with low and third-order turbulence closures. J Meteor Soc Jpn 86A:67–86

Cheng A, Xu K-M (2011) Improved low-cloud simulation from a multiscale modeling framework with a third-order turbulence closure in its cloud-resolving model component. J Geophys Res 116:D14101. https://doi.org/10.1029/2010JD015362

Cheng A, Xu K-M (2013a) Improving low-cloud simulation from an upgraded multiscale modeling framework model. Part III: tropical and subtropical cloud transitions over the northern Pacific. J Clim 26:5761–5781

Cheng A, Xu K-M (2013b) Diurnal variability of low clouds in the southeast Pacific simulated by an upgraded multiscale modeling framework model. J Geophys Res 118:9191–9208. https://doi.org/10.1002/jgrd.50683

Cheng A, Xu K-M, Stevens B (2010) Effects of resolution on the simulation of boundary-layer clouds and the partition of kinetic energy to subgrid scales. J Adv Model Earth Syst 2:3. https://doi.org/10.3894/JAMES.2010.2.3

Collins WD et al (2006) The formulation and atmospheric simulation of the Community Atmosphere Model Version 3 (CAM3). J Clim 19:2144–2161

Colman RA, McAvaney BJ (2011) On tropospheric adjustment to forcing and climate feedbacks. Clim Dyn 36:1649–1658. https://doi.org/10.1007/s00382-011-1067-4

DeAngelis AM, Qu X, Hall A (2016) Importance of vegetation processes for model spread in the fast precipitation response to CO_2 forcing. Geophys Res Lett 43:12,550–12,559. https://doi.org/10.1002/2016GL071392

Dong B, Gregory JM, Sutton RT (2009) Understanding land-sea warming contrast in response to increasing greenhouse gases, Part I: transient adjustment. J Clim 22:3079–3097

Doutriaux-Boucher M, Webb MJ, Gregory JM, Boucher O (2009) Carbon dioxide induced stomatal closure increases radiative forcing via a rapid reduction in low cloud. Geophys Res Lett 36:L02703. https://doi.org/10.1029/2008GL036273

Grabowski WW (2001) Coupling cloud processes with the large-scale dynamics using the cloud-resolving convection parameterization (CRCP). J Atmos Sci 58:978–997

Gregory J, Webb M (2008) Tropospheric adjustment induces a cloud component in CO_2 forcing. J Clim 21:58–71. https://doi.org/10.1175/2007JCLI1834.1

Hansen J, Lacis A, Rind D, Russell G, Stone P, Fung I, Ruedy R, Lerner J (1984) Climate sensitivity: Analysis of feedback mechanisms. In: Hansen JE, Takahashi T (eds) Climate processes and climate sensitivity, geophys. monogr, vol 29, pp 130–163. AGU, Washington, DC

Hansen J, Sato M, Ruedy R et al (2005) Efficacy of climate forcings. J Geophys Res 110:D18104. https://doi.org/10.1029/2005JD005776

Holtslag AAM, Boville BA (1993) Local versus nonlocal boundary layer diffusion in a global climate model. J Clim 6:1825–1842

Kamae Y, Watanabe M (2012) On the robustness of tropospheric adjustment in CMIP5 models. Geophys Res Lett 39:L23808. https://doi.org/10.1029/2012GL054275

Kamae Y, Watanabe M (2013) Tropospheric adjustment to increasing CO_2: its timescale and the role of land-sea contrast. Clim Dyn 41:3007–3024

Kamae Y, Watanabe M, Ogura T, Yoshimori M, Shiogama H (2015) Rapid adjustments of cloud and hydrological cycle to increasing CO_2: a review. Curr Clim Change Rep 1:103–113. https://doi.org/10.1007/s40641-015-0007-5

Kamae Y, Ogura T, Watanabe M, Xie S-P, Ueda H (2016) Robust cloud feedback over tropical land in a warming climate. J Geophys Res Atmos. https://doi.org/10.1002/2015/JD024525

Khairoutdinov MF, Randall DA (2001) A cloud resolving model as a cloud parameterization in the NCAR community climate system model: preliminary results. Geophys Res Lett 28:3617–3620

Khairoutdinov MF, Randall DA (2003) Cloud resolving modeling of the ARM summer 1997 IOP: model formulation, results, uncertainties, and sensitivities. J Atmos Sci 60:607–625

Klein SA, Hartmann DL (1993) The seasonal cycle of low stratiform clouds. J Clim 6:1587–1606

Merlis TM (2015) Direct weakening of tropical circulations from masked CO_2 radiative forcing. Proc Natl Acad Sci 112:13167–13171. https://doi.org/10.1073/pnas.1508268112

Myhre G, Highwood EJ, Shine KP, Stordal F (1998) New estimates of radiative forcing due to well mixed greenhouse gases. Geophys Res Lett 25:2715–2718. https://doi.org/10.1029/98GL01908

Painemal D, Xu K-M, Cheng A, Minnis P, Palikonda R (2015) Mean Structure and diurnal cycle of Southeast Atlantic boundary layer clouds: Insights from satellite observations and multiscale modeling framework simulations. J Clim 28:324–341. https://doi.org/10.1175/JCLI-D-14-00368.1

Randall DA, Xu K-M, Somerville RCJ, Iacobellis S (1996) Single-column models and cloud ensemble models as links between observations and climate models. J Clim 9:1683–1697

Randall D, Khairoutdinov M, Arakawa A, Grabowski WW (2003) Breaking the cloud parameterization deadlock. Bull Am Meteorol Soc 84:1547–1564

Rayner NA, Parker DE, Horton EB, Folland CK, Alexander LV, Rowell DP, Kent EC, Kaplan A (2003) Global analyses of sea surface temperature, sea ice, and night marine air temperature since the late nineteenth century. J Geophys Res 108:4407. https://doi.org/10.1029/2002JD002670

Ringer MA, Andrews T, Webb MJ (2014) Global-mean radiative feedbacks and forcing in atmosphere-only and coupled atmosphere-ocean climate change experiments. Geophys Res Lett 41:4035–4042. https://doi.org/10.1002/2014GL060347

Shaw TA, Voigt A (2016) Land dominates the regional response to CO_2 direct radiative forcing. Geophys Res Lett 43:11,383–11,391. https://doi.org/10.1002/2016GL071368

Sherwood SC, Bony S, Boucher O, Bretherton CS, Forester PM, Gregory JM, Stevens B (2015) Adjustments in the forcing-feedback framework for understanding climate change. Bull Am Meteor Soc 96:217–228. https://doi.org/10.1175/BAMS-D-13-00167.1

Soden BJ, Vecchi GA (2011) The vertical distribution of cloud feedback in coupled ocean-atmosphere models. Geophys Res Lett 38:L12704. https://doi.org/10.1029/2011GL047632

Stan C, Xu L (2014) Climate simulations and projections with the super-parameterized CCSM4. Environ Model Softw 60:1234–1252. https://doi.org/10.1016/j.envsoft.2014.06.013

Vial J, Dufresne J-L, Bony S (2013) On the interpretation of inter-model spread in CMIP5 climate sensitivity estimates. Clim Dyn. https://doi.org/10.1007/s00382-013-1725.9

Watanabe M et al (2012) Fast and slow timescales in the tropical low-cloud response to increasing CO_2 in two climate models. Clim Dyn 39:1627–1641. https://doi.org/10.1007/s00382-011-1178-y

Webb MJ, Lambert FH, Gregory JM (2013) Origins of differences in climate sensitivity, forcing and feedback in climate models. Clim Dyn 40:677–707

Wood R, Bretherton CS (2006) On the relationship between stratiform low cloud cover and lower-tropospheric stability. J Clim 19:6425–6432. https://doi.org/10.1175/JCLI3988.1

Wyant MC, Khairoutdinov M, Bretherton CS (2006) Climate sensitivity and cloud response of a GCM with a superparameterization. Geophys Res Lett 33:L06714. https://doi.org/10.1029/2005GL025464

Wyant MC, Bretherton CS, Blossey PN, Khairoutdinov M (2012) Fast cloud adjustment to increasing CO_2 in a superparameterized climate model. J Adv Model Earth Syst 4:M05001. https://doi.org/10.1029/2011MS000092

Xu K-M, Cheng A (2013a) Evaluating low-cloud simulation from an upgraded multiscale modeling framework model, Part I: sensitivity to spatial resolution and climatology. J Clim 26:5717–5740

Xu K-M, Cheng A (2013b) Evaluating low-cloud simulation from an upgraded multiscale modeling framework model, Part II: seasonal variations over the eastern Pacific. J Clim 26:5741–5760

Xu K-M, Cheng A (2016) Understanding the tropical cloud feedback from an analysis of the circulation and stability regimes simulated from an upgraded multiscale modeling framework. J Adv Model Earth Syst 8:1825–1846. https://doi.org/10.1002/2016MS000767

Xu K-M, Li Z, Cheng A, Blossey PN, Stan C (2017) Differences in the hydrological cycle and sensitivity between multiscale modeling frameworks with and without a higher-order turbulence closure. J Adv Model Earth Syst 9:2120–2137. https://doi.org/10.1002/2017MS000970

Yang F, Kumar A, Schlesinger ME, Wang W (2003) Intensity of hydrological cycles in warmer climates. J Clim 16:2419–2423

Zelinka MD, Klein SA, Taylor KE, Andrews T, Webb MJ, Gregory JM, Forster PM (2013) Contributions of different cloud types to feedbacks and rapid adjustment in CMIP5. J Clim 26:5007–5027. https://doi.org/10.1175/JCLI-D-12-00555.1